Nano-metallic glasses: size reduction brings ductility, surface state drives its extent

D.Z. Chen[*,1], D. Jang[1], K.M. Guan[2], Q. An[3], W.A. Goddard, III[3], and J.R. Greer[1,4],

[1]Division of Engineering and Applied Sciences, California Institute of Technology, Pasadena CA, 91106
[2]Department of Chemistry and Chemical Engineering, California Institute of Technology, Pasadena CA, 91106
[3]Materials and Process Simulation Center, California Institute of Technology, Pasadena CA, 91125
[4]The Kavli Nanoscience Institute, California Institute of Technology, Pasadena CA, 91106

1. Supporting Figures:

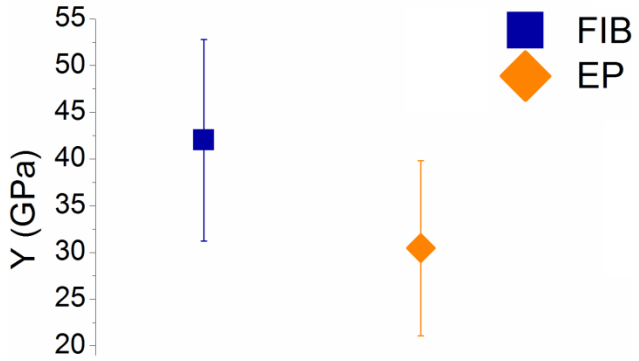

Figure S1: Average Young's moduli for FIB and EP samples across ten independent specimens (five of each type). EP samples show a slightly lower modulus, but it is within one standard deviation.

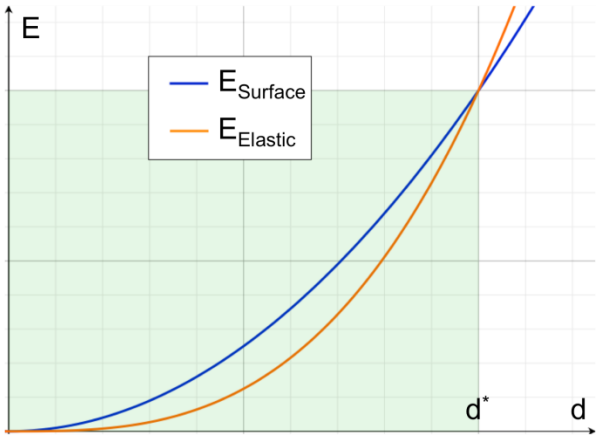

Figure S2: Graph depicting the d^2 versus d^3 scaling argument for surface energy, $E_{Surface}$ and total stored elastic energy, $E_{Elastic}$. At diameters lower than d* (opaque green region), the energy required for a crack/fracture to initiate at the surface ($E_{Surface}$) dominates, and shear banding is suppressed. Altering the surface state increases the gap between $E_{Surface}$ and $E_{Elastic}$, further suppressing catastrophic failure.

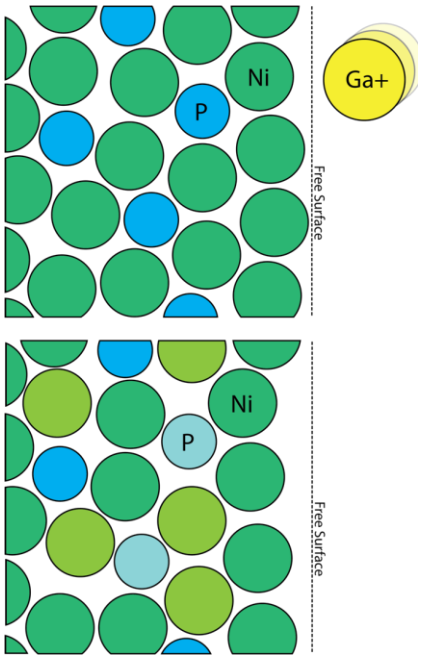

Figure S3—Diagram depicting the generation of high potential energy atoms from ion irradiation for a typical binary MG system. Top: as-cast configuration of NiP MG atoms, with the free surface to the right of the depicted atoms (not shown). Ga ions impinge upon the free surface from the right. Bottom: atoms rearrange after collision, resulting in high potential energy atoms—shown in light green for Ni and light blue for P. The free volume in the vicinity of these atoms is notably higher, creating an easy path for them to take in response to elastic energy input.

2. Supporting Methods

Synthesis

Electroplated (EP) samples were fabricated following a template pattern transfer procedure described in.[1] In this methodology, a thin layer of Au (~100 nm) is first evaporated onto a silicon wafer coated with a 30nm-thick Ti layer without breaking the vacuum. The ~700nm-thick PMMA is then spin-coated onto this seed layer, patterned using e-beam lithography, and developed to reveal vertical through-holes with the desired diameters. The electroplating is performed by providing a constant current between the anode (Ni foil) and the cathode (prepared template and Au dummy chip), and tension samples are made by overplating the metallic glass above the PMMA surface. Table 2 provides details on the specific Ni-P electroplating conditions. More details about this fabrication method for other metallic nano structures can be found in [1].

In addition to such templated electroplating, a blanket ~2µm-thick Ni-P film was electroplated directly onto the seed layer as a separate Si chip. This film had virtually identical composition to the nano-pillars (Table 2 and Figure 2f). Tensile samples with ~100-nm and 500-nm diameters and ~650-nm and 2-µm gauge lengths were then fabricated from an electroplated NiP film using an FEI Nova 200 Nanolab focused ion beam with a final etching condition of 30kV/10pA (Figure 3). Great care was taken when carving the heads of the tension samples to minimize bending during nano-mechanical testing.

Tensile Testing

A custom-made *in situ* SEM, SEMentor (SEM + nanoindenter), was used to conduct the nanomechanical tension tests.[2] The nanoindentor arm is fitted with a diamond Berkovich tip that

was carefully milled with FIB into the shape and dimensions of a tensile grip, as seen partially in Figure 3. All of the experiments were carried out at a constant nominal displacement rate (0.5-8 nms^{-1}) using a feedback algorithm, which results in a global strain rate of $1.0e^{-3}s^{-1}$. The raw load-displacement data were recorded after isolating the specimen-only response from the load frame, support spring, and substrate compliances. Engineering stress and strain values were then calculated from load-displacement data using the sample diameters measured from SEM images.

Molecular Dynamics

We started with a Ni_3Al crystal with a total of 4000 atoms and melted the system at 3000 K. Then 5% of the Al atoms were replaced by Ni atoms to form a $Ni_{80}Al_{20}$ liquid. Periodic boundary conditions were applied in all three directions of the simulation box to eliminate surface effects. Equations of motion were solved using the velocity Verlet algorithm with a time step of 1 femtosecond. The dynamics were carried out with an NPT ensemble (constant particles, pressure, and temperature) using a Nose-Hoover thermostat (time constant of 0.1 picosecond) and barostat (time constant of 1 picosecond).

In addition to the steps mentioned in the main text of the paper, periodic boundary conditions were applied only along the cylinder axis during quenching. Additionally, the length of the cylinder was fixed during this step as well. The irradiation step was performed using an NVE ensemble (constant particles, volume, and energy) for 200 picoseconds until the potential energy of the system stabilized. After this the irradiated pillars were immediately quenched to room temperature and relaxed using an NVT ensemble (constant particles, volume, and temperature) for 500 picoseconds. To avoid an unphysical attraction in this high-energy collision process, we applied a truncated and shifted Leonard-Jones pairwise interaction to the original

EAM potential in the repulsive region. The form and parameters of the LJ potential are identical to that of Xiao, et al.[3] Uniaxial tension was conducted by rescaling the simulation box along the loading direction. The atomic stresses were obtained from the atomic virial[4] to extract the total stresses of the nanopillars.

The simulated irradiation fluence value of 0.0625/nm^2 was obtained from a back-of-the-envelope calculation using experimental FIB conditions on the FEI Nova 200 NanoLab DualBeam^{TM} SEM/FIB. The dwell time for the beam was 1 μs, and the spot size was 2 nm^2. From these two parameters, we can use eq. (1) to estimate the number of scans per milling session, given the user-specified FIB pattern area and a correction to the scan area for the 50% overlap in beam spot in both the x and y directions. From this estimate of the number of scans per session, we can use eq. (2) to obtain the ion fluence by applying the number of ions per second needed to achieve an ion current of 10 pA, which results in a value of ~0.0625/nm^2.

$$N_{Scans} = \frac{t_{Final}}{(\frac{A_{FIB}}{A_{Spot}} * 2t_{Dwell})} \quad (1)^{*}$$

*: The factor 2 corresponds to a correction to the scan area for the 50% overlap in the beam spot for the x and y directions. A_{Spot} is the spot size, A_{FIB} is the total pattern area, t_{Final} is the final exposure time, and t_{Dwell} is the total dwell time.

$$\Phi = \frac{I_{Ion} * t_{Sample}}{-e} * N_{Scans} \Big/ 10A_{FIB-affected} \quad (2)^{**}$$

**: The factor 10 corresponds to a rough correction for the glancing angle of incidence for the incoming ion beam. I_{Ion} is the ion current, t_{Sample} is the FIB exposure time on the sample surface, e is the electron charge, and $A_{FIB\text{-}afffected}$ is the cross-sectional area of the FIB-affected zone on the sample surface.

3. Supporting Discussion:

Short range order (SRO)

A Ni-P system was chosen because it lends itself well to electroplating. NiP metallic glasses may have different short range order (SRO) compared with the more common binary glass, CuZr, which has more metallic-like bonding.[5] Although the bonding between Ni and P may not be purely metallic, it should not adversely affect the role of Ni-P metallic glass as a model system nor does it change the findings or the conclusions of this work. Neutron diffraction experiments have also suggested that the pair distribution functions (PDFs) of metal-metalloid systems are qualitatively similar to metal-metal systems such as CuZr, especially after the second nearest neighbors.[6] It is not known whether the brittle-to-ductile transition occurs in only metallic glass systems or in other amorphous systems as well. A similar phenomenon has been seen in amorphous silica nanowires, which at 50-100nm diameters undergo brittle failure[7] and at down to 20nm exhibit great deformability[8]. The Cu-Zr which was shown to undergo the size-induced brittle-to-ductile transition (ref. 10 in the manuscript) has more of a metallic-type bonding, but cannot be considered to be purely metallic. Theoretically, the glass formability of a purely metallic bonding system is basically zero—for example a slab of pure Cu or pure Ni cannot be made to be amorphous. Typically, a certain amount of covalent bonding or orientation preference is needed for the formation of an amorphous microstructure. Additionally, the microstructure of our NiP system is completely amorphous, as validated by TEM, and, as Argon et al.'s (ref. 25 in the manuscript) experiments have shown, even unrelated analogous systems such as bubble rafts can lead to rather applicable insights to the underlying deformation in amorphous systems, including metallic glasses.

Electroplating

The rate of metal ion deposition during electroplating was fairly consistent for both the films and the 100-nm template pillars, suggesting that the plating time is independent of template feature size. Even at 100nm-diameters, the electroplating remained reasonably unhindered by the template, which implies that the only relevant driving force for plating rate is the current density. From the SEM images, it can also be seen in Figure 3-b & c that the electroplated pillars had relatively smooth surfaces, with few hydrogen bubbles, which are a common issue with electroplated samples.[9] Tensile specimens also have characteristic caps, which are a result of plating over the e-beam developed features. These caps are quite isotropic, and somewhat resemble mushroom tops. Isotropy in the overplated caps is an indicator for the presence of an amorphous rather than a crystalline phase, which might show some sort of anisotropy or orientation preference, as we have seen with our previous samples.[1]

Carbon and Oxygen contamination

EDX only detects the surface atoms, and due to the small size of the EP specimen, the spot size of the e-beam actually includes some of the atoms on the template surface as well as those on the specimens. We have re-normalized the chemical compositions based only on the relative Ni and P content to reflect this. The resulting difference in relative P content is less than 1 wt% between the two sample types, which makes them be nominally identical in terms of chemical composition, as planned. As mentioned in the manuscript, the O and C present on the surfaces of the samples should not form continuous layers, and as such do not bear any load. It

may affect the straining slightly, but it is highly unlikely to induce plastic flow in an otherwise brittle glass.

Strain from in-situ video

Raw data obtained from the displacement signal of the nanoindenter produces results which have high variability in the loading moduli, an unavoidable characteristic detriment of nano-mechanical testing. Many factors can affect the apparent modulus: slight misalignments between the sample and the grip, surface imperfections on the sample or the grip (bumps), the machine compliance, the imperfect adhesion, etc. to name a few. We have carefully re-examined the raw data and used the frames from the in-situ SEM videos rather than the displacement signal from the nanoindenter to measure and recalibrate the strains obtained in the mechanical data. This technique is more reliable for strain determination and has been successfully utilized in many publications from our group.[10-12] Such a discrepancy between the strain based on video frames and that measured in the nanoindenter is typical and likely stems from the effects of machine and grip compliances in both sample types and additional substrate effects in EP samples.

References

1. Burek, M. J.; Greer, J. R. *Nano Lett* **2010,** 10, (1), 69-76.
2. Kim, J. Y.; Greer, J. R. *Acta Mater* **2009,** 57, (17), 5245-5253.
3. Xiao, Q. R.; Huang, L. P.; Shi, Y. F. *J Appl Phys* **2013,** 113, (8).
4. Lutsko, J. F. *J Appl Phys* **1989,** 65, (8), 2991-2997.
5. Cheng, Y. Q. D., J.; Ma, E. *Materials Research Letters* **2013,** 1, (1), 3-12.
6. Ma, D.; Stoica, A. D.; Wang, X. L. *Nat Mater* **2009,** 8, (1), 30-34.
7. Ni, H.; Li, X. D.; Gao, H. S. *Appl Phys Lett* **2006,** 88, (4).
8. Tong, L. M.; Lou, J. Y.; Ye, Z. Z.; Svacha, G. T.; Mazur, E. *Nanotechnology* **2005,** 16, (9), 1445-1448.
9. Hoare, J. P. *J Electrochem Soc* **1986,** 133, (12), 2491-2494.
10. Gu, X. W.; Loynachan, C. N.; Wu, Z. X.; Zhang, Y. W.; Srolovitz, D. J.; Greer, J. R. *Nano Lett* **2012,** 12, (12), 6385-6392.
11. Jang, D.; Greer, J. R. *Nat Mater* **2010,** 9, (3), 215-219.
12. Landau, P.; Guo, Q.; Hattar, K.; Greer, J. R. *Adv Funct Mater* **2013,** 23, (10), 1281-1288.